

Natural convection in a porous trapezoidal enclosure with magneto-hydrodynamic effect

M.A.H. Mamun¹, Md.T. Islam², Md.M. Rahman³

¹Department of Mechanical Engineering
Bangladesh University of Engineering and Technology (BUET)
Dhaka-1000, Bangladesh

²Department of Mechanical Engineering, Wayne State University
Detroit, MI 48202, USA

³Department of Mathematics
Bangladesh University of Engineering and Technology (BUET)
Dhaka-1000, Bangladesh
mmustafizurrahman@math.buet.ac.bd; m71ra@yahoo.com

Received: 2009-08-25 **Revised:** 2010-03-31 **Published online:** 2010-06-01

Abstract. The effects of magnetic force, acting vertically downward on natural convection within a porous trapezoidal enclosure saturated with an electrically conducting fluid have been investigated numerically. The bottom wall of the enclosure is subjected to a constant hot temperature and the top wall experiences a constant cold temperature whereas the remaining sidewalls are kept adiabatic. The physical problems are represented mathematically by different sets of governing equations along with the corresponding boundary conditions. By using Galerkin weighted residual method of finite element formulation, the non-dimensional governing equations are discretized. For natural convection in a porous medium the influential parameters are the modified Rayleigh number Ra_m , the fluid Rayleigh number Ra_f , the inclination angle of the sidewalls of the cavity γ , the rotational angle of the enclosure Φ and the Hartmann number Ha , through which different thermo-fluid characteristics inside the enclosure are obtained. In the present study, the obtained results are presented in terms of streamlines, isotherms and average Nusselt number along the hot wall. The result shows that with increasing Ha , the diffusive heat transfer become prominent even though the modified Rayleigh number increases. Optimum heat transfer rate is obtained at higher values of Ra_m in the absence of magnetic force.

Keywords: magneto-hydrodynamics, optimization, permeability, Hartmann number, fluid Rayleigh number, modified Rayleigh number.

Nomenclature

B_0 downward component of the magnetic force [Wb/m²] C_p specific heat at constant pressure [J/kg K]

Da	Darcy number	T	temperature of the fluid [$^{\circ}C$]
g	gravitational acceleration [m/s^2]	u	velocity component at x -direction [m/s]
h	convective heat transfer coefficient [$W/m^2 K$]	U	dimensionless velocity component at X -direction
Ha	Hartmann number	\bar{v}	velocity vector
K_f	thermal conductivity of the fluid [$W/m K$]	v	velocity component at y -direction [m/s]
K_m	thermal conductivity of the porous media [$W/m K$]	V	dimensionless velocity component at Y -direction
Nu	Nusselt number	W	length of the cavity [m]
Pr	Prandtl number	x	distance along the x -coordinate
R	length of the inclined sidewalls [m]	X	distance along the non-dimensional x -coordinate
R_k	ratio of thermal conductivity of solid and fluid [K_m/K_f]	Y	distance along the non-dimensional y -coordinate
Ra_f	fluid Rayleigh number		
Ra_m	modified Rayleigh number		

Greek symbols

α_f	thermal diffusivity of the fluid [m^2/s]	$\bar{\mu}$	effective viscosity [$Pa s$]
β_f	volumetric coefficient of thermal expansion [K^{-1}]	ν_f	kinematic viscosity of the fluid [m^2/s]
γ	inclination angle of the sidewalls of the cavity	ρ_f	density of the fluid [kg/m^3]
θ	dimensionless temperature	σ_e	fluid electrical conductivity [$\Omega^{-1}m^{-1}$]
κ	permeability of porous medium [m^2]	φ	electrical potential
μ_f	dynamic viscosity of the fluid [$Pa s$]	Φ	rotational angle of the cavity
		Ψ	dimensionless stream function
		Ω	dimensionless vorticity function

Subscripts

av	average value	H	value of hot temperature
c	value of cold temperature		

Superscripts

t	cavity mounted on the top surface of the container	s	cavity mounted on the side surface of the container
-----	--	-----	---

1 Introduction

Heat transfer through saturated porous media is an important development and an area of very rapid growth in contemporary trend of heat transfer research. A porous medium consists of a solid matrix with an interconnected void. This solid matrix is either rigid or deformable [1]. Porous materials such as sand and crushed rock underground saturated

with water, which, under the influence of local pressure gradients, migrates and transports energy through the material. Natural convection heat transfer in a cavity saturated with porous media in the presence of magnetic field is a new branch of thermo-fluid mechanics. The heat transport phenomenon can be described by means of the hydrodynamics, the convective heat transfer mechanism and the electromagnetic field as they have a symbiotic relationship [2–6].

The flow within an enclosure consisting of two horizontal walls, at different temperatures, is an important circumstance encountered quite frequently in practice. In all the applications having this kind of situation, heat transfer occurs due to the temperature difference across the fluid layer, one horizontal solid surface being at a temperature higher than the other. If the upper plate is the hot surface, then the lower surface has heavier fluid and by virtue of buoyancy the fluid would not come to the lower plate. Because in this case the heat transfer mode is restricted to only conduction. But if the fluid is enclosed between two horizontal surfaces of which the upper surface is at lower temperature, there will be the existence of cellular natural convective currents, which are called as Benard cells. For fluids whose density decreases with increasing temperature, this leads to an unstable situation. Benard [7] mentioned this instability as a “top heavy” situation. In that case fluid is completely stationary and heat is transferred across the layer by the conduction mechanism only. Rayleigh [8] recognized that this unstable situation must break down at a certain value of Rayleigh number above which convective motion must be generated. Jeffreys [9] calculated this limiting value of Ra to be 1708, when air layer is bounded on both sides by solid walls. Magneto-hydrodynamics (MHD) is the science of the motion of electrically conducting fluids under the influence of applied magnetic forces. The symbiotic interaction between the fluid velocity field and the electromagnetic forces give rise to a flow scenarios; the magnetic field affects the motion.

Natural convection in an enclosure saturated with porous medium plays a significant role in many practical applications. Among those, geophysical systems: heat exchange between soil and atmosphere, dynamics of terrestrial heat flow through aquifer; compacted beds for the chemical industry, high performance insulations for cryogenic containers, sensible heat storage beds, food processing, grain storage, solar power collectors, flows over heat exchanger pipes, cooling of electronic systems, cooling of radioactive waste containers and the post-accidental heat removal in nuclear reactors have become increasingly important to the engineers and scientists.

In this analysis, The effects of permeability and different thermal boundary conditions on the natural convection in a square porous cavity by using Darcy–Forchheimer model [10] and Darcy–Brinkman-Forchheimer model [11, 12] have been studied numerically. The tilted position of the enclosure [13–15] has a significant influence on the natural convection. Mahmud and Fraser [16] examined the flow, temperature and entropy generation fields inside a square porous cavity under the influence of magnetic field using Darcy model. The momentum equation including Navier–Stokes inertia term and Brinkman viscous diffusion term derived for the porous media in the presence of magnetic field makes the present works discernible. The main attribute for choosing the trapezoidal shape cavity is to enhance the heat transfer rate as it could be said intuitively due to its extended cold top surface. Contextually the present study will focus on the computational

analysis of the influence of magnetic field on the natural convection in a trapezoidal enclosure saturated with porous medium of constant porosity.

2 Selection of the base model

Brinkman's extension of Darcy's law was checked by Lundgren [17] by measuring the flows through cubic arrays of spherical beads on wires. The experimental results matched with the Brinkman formula for permeability as a function of porosity. Levy [18] reported that the fluid filtration is governed by the Brinkman's equation for smaller particles whereas the Darcy model is valid for coarse particles. There is some uncertainty about the validity of the Forchheimer model for fine particles. Contextually, the Darcy–Brinkman model has been taken in the present study.

2.1 Darcy–Brinkmann model

An alternative to Darcy's equation is Brinkmann's equation which accounts for the transition from Darcy flow to highly viscous flow, in the limit of extremely high permeability.

$$\nabla p = -\frac{\mu}{\kappa}\bar{v} + \bar{\mu}\nabla^2\bar{v}. \quad (1)$$

The first term is the usual Darcy term and the second is analogous to the Laplacian term that appears in the Navier-Stokes equation. The coefficient $\bar{\mu}$ is an effective viscosity. In general μ and $\bar{\mu}$ are approximately equal.

2.2 Electromagnetic field in hydrodynamics

Electromagnetic field has an important influence on the hydrodynamics. One of the main purposes of the electromagnetic control is to stabilize the flow and suppress oscillatory instabilities, which degrades the resulting crystal. To incorporate the electromagnetic force with the fluid flow model, the Lorentz force for moving axes has been taken in consideration.

$$\bar{F} = q\bar{E} + \bar{j} \times \bar{B}, \quad (2)$$

$$\bar{j} = \sigma_e(\bar{E} + \bar{v} \times \bar{B}), \quad (3)$$

where \bar{j} is the current density, σ_e is the electrical conductivity of the fluid and $\bar{E} = -\nabla\varphi$ is the electric field and φ is the electric potential and \bar{v} is the field velocity. Electrical insulation is present in the practical applications. So $\nabla\varphi$ becomes zero (i.e. $\nabla\varphi = 0$) indicating the absence of the electric field. Now the modified Lorentz force becomes

$$\bar{F}_m = \sigma_e(\bar{v} \times \bar{B}) \times \bar{B}. \quad (4)$$

Therefore the magnetohydrodynamic (MHD) flow model has been formulated as:

$$\rho_f(\bar{v}\nabla) \cdot \bar{v} = -\nabla p + \mu_f\nabla^2\bar{v} - \frac{\mu_f}{\kappa}\bar{v} + \sigma_e(\bar{v} \times \bar{B}) \times \bar{B} + \bar{F}_B, \quad (5)$$

where \bar{F}_B is body force, μ_f and ρ_f are dynamic viscosity and density of fluid respectively.

3 Physical model

The physical model considered here is shown in Fig. 1, along with the important geometric parameters. It consists of a trapezoidal cavity with an electrically conducting fluid saturated porous medium, whose bottom wall and top wall are subjected to hot T_H and cold T_C temperatures respectively while the side walls are kept adiabatic. Natural convection flow of a thermal viscous fluid assumed to be Newtonian is considered under the Oberbeck–Boussineq approximation in the presence of a gravitational field. The Oberbeck–Boussineq approximation is based on the assumptions that the temperature variations are small enough in order to consider the density ρ as a constant except in the buoyancy term $\rho\bar{g}$, where \bar{g} is the gravitational force and ρ is given linearly by $\rho = \rho_0[1 - \beta(T - T_0)]$ where T is the temperature and ρ_0 and T_0 denote reference density and temperature respectively. The density change due to changes in pressure is neglected. Fluid properties such as viscosity μ , the permeability κ , thermal expansion $\beta = -\frac{1}{\rho_0}(\frac{\partial\rho}{\partial T})_p$, the thermal diffusivity η and the specific heat C_p are assumed to be constants. Porous inertia effect is neglected while viscous effect is considered. Applied magnetic force is acting along the direction of the gravity. Here the Prandtl number is assumed to be unity.

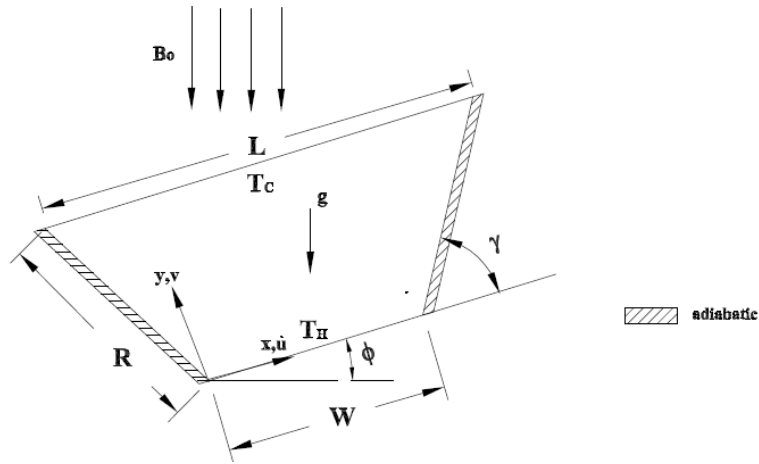


Fig. 1. Schematic diagram of the physical system.

4 Mathematical model

Buoyancy driven flow of an electrically conducting fluid inside a trapezoidal enclosure packed with a porous media is analogue to Rayleigh–Benard multi-cellular convective transport phenomenon. Natural convection heat transfer within such an enclosure is a function of the temperature difference between the hot and cold walls, the boundary

conditions, the inclination angle of the side walls of the cavity, the rotational angle of the cavity, the permeability of the porous medium, magnitude and direction of the applied magnetic fields and the properties of the electrically conducting fluid flow.

The generalized governing equations are used based on the conservation laws of mass, momentum and energy. As the heat transfer depends upon a number of factors, a dimensional analysis is presented to show the important non-dimensional parameters, which will influence the dimensionless heat transfer parameter, i.e. Nusselt number.

4.1 Governing equations

Non-dimensional parameters used for making the governing equations dimensionless are stated as follows:

$$X = \frac{x}{W}; Y = \frac{y}{W}; U = \frac{uW}{\alpha_f}; V = \frac{vW}{\alpha_f}; \theta = \frac{T - T_C}{T_H - T_C};$$

$$Ra_f = \frac{g\beta_f(T_H - T_C)W}{\alpha_f\nu_f}; Pr = \frac{\nu_f}{\alpha_f}; Da = \frac{\kappa}{W^2}; Ha = B_0\sqrt{\frac{\sigma_e\kappa}{\mu_f}}.$$

Continuity equation

$$\frac{\partial^2\Psi}{\partial X\partial Y} - \frac{\partial^2\Psi}{\partial X\partial Y} = 0. \quad (6)$$

Momentum equation

$$\left(\frac{\partial\Psi}{\partial Y}\frac{\partial\Omega}{\partial X} - \frac{\partial\Psi}{\partial X}\frac{\partial\Omega}{\partial Y}\right)$$

$$= Pr\left(\frac{\partial^2\Omega}{\partial X^2} + \frac{\partial^2\Omega}{\partial Y^2}\right) - \frac{Pr}{Da}\Omega + Ra Pr\left(\frac{\partial\theta}{\partial X}\cos\Phi - \frac{\partial\theta}{\partial Y}\sin\Phi\right)$$

$$- \frac{Ha^2 Pr}{Da}\left\{\frac{\partial^2\Psi}{\partial X^2}\sin^2\Phi + \frac{\partial^2\Psi}{\partial Y^2}\cos^2\Phi + 2\frac{\partial^2\Psi}{\partial X\partial Y}\sin\Phi\cos\Phi\right\}. \quad (7)$$

Energy equation

$$\frac{\partial\Psi}{\partial Y}\frac{\partial\theta}{\partial X} - \frac{\partial\Psi}{\partial X}\frac{\partial\theta}{\partial Y} = \frac{\partial^2\theta}{\partial X^2} + \frac{\partial^2\theta}{\partial Y^2}. \quad (8)$$

4.2 Boundary conditions

Bottom wall: $\Psi=0; \theta=1$ at $0 \leq X \leq 1$ and $Y = 0$.

Top wall: $\Psi=0; \theta=0$ at $-\frac{R}{W}\cos\gamma \leq X \leq \left(1 + \frac{R}{W}\cos\gamma\right)$ and $Y = \frac{R}{W}\sin\gamma$.

Side wall: $\Psi=0; \frac{\partial\theta}{\partial\bar{S}}=0$ at $0 \leq |\bar{S}| \leq \frac{R}{W}$, where $\bar{S} = X\hat{i} + Y\hat{j}$.

Non-dimensional heat transfer parameter Nusselt number is stated as:

$$Nu_{av} = \int_0^W \frac{h(x)x}{k} dx, \quad (9)$$

$$Nu_{av} = \int_0^1 \left(\frac{\partial \theta}{\partial Y} \right)_{Y=0} dX. \quad (10)$$

4.3 Finite element formulations

The quadratic interpolation function has been considered for the stream function, the vorticity function and the non-dimensional temperature.

$$\Psi(X, Y) = N_j^e \Psi_j^e, \quad (11)$$

$$\Omega(X, Y) = N_j^e \Omega_j^e, \quad (12)$$

$$\theta(X, Y) = N_j^e \theta_j^e, \quad (13)$$

where $j = 1, 2, 3, \dots, 6, N_j$, are the element interpolation functions.

The considered triangular element has six nodes. Therefore the interpolation functions are six noded trigular shape functions. All six nodes are associated with the stream function, the vorticity function and the non-dimensional temperature.

To derive the finite element equations, the method of weighted residuals [19] is applied to the equations to the equations (6)–(8) and the Gauss's theorem is applied to generate the boundary integral terms associated with the surface tractions.

Continuity equation

$$\begin{aligned} \frac{\partial^2 \Psi}{\partial X \partial Y} - \frac{\partial^2 \Psi}{\partial X \partial Y} &= 0 \quad (14) \\ \Rightarrow \int_{\Lambda^e} \left(\frac{\partial^2 \Psi}{\partial X \partial Y} - \frac{\partial^2 \Psi}{\partial X \partial Y} \right) N_i d\Lambda^e &= 0 \\ \Rightarrow \int_{\Lambda^e} \left[\frac{\partial}{\partial X} \left(\frac{\partial \Psi}{\partial Y} \right) - \frac{\partial}{\partial Y} \left(\frac{\partial \Psi}{\partial X} \right) \right] N_i d\Lambda^e &= 0 \\ \Rightarrow \int_{\Lambda^e} \left(- \frac{\partial N_i^e}{\partial X} \frac{\partial N_j^e}{\partial Y} - \frac{\partial N_i^e}{\partial Y} \frac{\partial N_j^e}{\partial X} \right) \Psi_j^e d\Lambda^e \\ &+ \int_{\Gamma^e} \left(\frac{\partial \bar{\Psi}}{\partial Y} - \frac{\partial \bar{\Psi}}{\partial X} \right) N_i^e d\Gamma^e = 0, \quad (15) \end{aligned}$$

where A^e is the element area and Γ^e is the element boundary condition.

The elements of the local matrices are as follow:

$$A_{ij}^{11} = \int_{\Lambda^e} \left(-\frac{\partial N_i^e}{\partial X} \frac{\partial N_j^e}{\partial Y} + \frac{\partial N_i^e}{\partial Y} \frac{\partial N_j^e}{\partial X} \right) d\Lambda^e,$$

$$A_{ij}^{12} = A_{ij}^{13} = 0,$$

$$f_{i_1}^e = - \int_{\Gamma^e} \left(\frac{\partial \bar{\Psi}}{\partial Y} - \frac{\partial \bar{\Psi}}{\partial X} \right) N_i^e d\Gamma^e.$$

Similarly, for momentum equation the elements of the local matrices are:

$$A_{ij}^{21} = -\frac{Ha^2 Pr}{Da} \int_{\Lambda^e} \left\{ \frac{\partial N_i^e}{\partial X} \frac{\partial N_j^e}{\partial X} \sin^2 \Phi + \frac{\partial N_i^e}{\partial Y} \frac{\partial N_j^e}{\partial Y} \cos^2 \Phi \right. \\ \left. + \left(\frac{\partial N_i^e}{\partial X} \frac{\partial N_j^e}{\partial Y} + \frac{\partial N_i^e}{\partial Y} \frac{\partial N_j^e}{\partial X} \right) \sin \Phi \cos \Phi \right\} d\Lambda^e,$$

$$A_{ij}^{22} = \frac{Pr}{Da} \int_{\Lambda^e} N_i^e d\Lambda^e + Pr \int_{\Lambda^e} \left(\frac{\partial N_i^e}{\partial X} \frac{\partial N_j^e}{\partial X} + \frac{\partial N_i^e}{\partial Y} \frac{\partial N_j^e}{\partial Y} \right) d\Lambda^e,$$

$$A_{ij}^{23} = Ra Pr \int_{\Lambda^e} \left(\frac{\partial N_i^e}{\partial Y} \sin \Phi - \frac{\partial N_j^e}{\partial X} \cos \Phi \right) N_i^e d\Lambda^e,$$

$$f_{i_2}^e = \int_{\Gamma^e} N_i^e \left\{ \left(\frac{\partial \bar{\Omega}}{\partial X} + \frac{\partial \bar{\Omega}}{\partial Y} \right) - \left(\frac{\partial \bar{\Psi}}{\partial X} + \frac{\partial \bar{\Psi}}{\partial Y} \right) \sin \Phi \cos \Phi \right. \\ \left. - \frac{\partial \bar{\Psi}}{\partial X} \sin^2 \Phi - \frac{\partial \bar{\Psi}}{\partial Y} \cos^2 \Phi \right\} d\Gamma^e \\ - \int_{\Gamma^e} \left(\sum_{j=1}^6 \Psi_j^e \frac{\partial N_j^e}{\partial Y} \sum_{k=1}^6 \Omega_k^e \frac{\partial N_k^e}{\partial X} - \sum_{j=1}^6 \Psi_j^e \frac{\partial N_j^e}{\partial X} \sum_{k=1}^6 \Omega_k^e \frac{\partial N_k^e}{\partial Y} \right) N_i^e d\Lambda^e.$$

Similarly, for energy equation the elements of the local matrices are:

$$A_{ij}^{31} = A_{ij}^{32} = 0,$$

$$A_{ij}^{33} = \int_{\Lambda^e} \left(\frac{\partial N_i^e}{\partial X} \frac{\partial N_j^e}{\partial X} + \frac{\partial N_i^e}{\partial Y} \frac{\partial N_j^e}{\partial Y} \right) d\Lambda^e,$$

$$f_{i_3}^e = \int_{\Gamma^e} N_i^e \left(\frac{\partial \bar{\theta}}{\partial X} + \frac{\partial \bar{\theta}}{\partial Y} \right) d\Gamma^e \\ - \int_{\Lambda^e} \left(\sum_{j=1}^6 \Psi_j^e \frac{\partial N_j^e}{\partial Y} \sum_{k=1}^6 \theta_k^e \frac{\partial N_k^e}{\partial X} - \sum_{j=1}^6 \Psi_j^e \frac{\partial N_j^e}{\partial X} \sum_{k=1}^6 \theta_k^e \frac{\partial N_k^e}{\partial Y} \right) d\Lambda^e.$$

$$K_{ij}^e = \begin{bmatrix} A_{ij}^{11} & A_{ij}^{12} & A_{ij}^{13} \\ A_{ij}^{21} & A_{ij}^{22} & A_{ij}^{23} \\ A_{ij}^{31} & A_{ij}^{32} & A_{ij}^{33} \end{bmatrix}; \quad a_i^e = \begin{bmatrix} \Psi_i^e \\ \Omega_i^e \\ \theta_i^e \end{bmatrix}; \quad f_i^e = \begin{bmatrix} f_{i1}^e \\ f_{i2}^e \\ f_{i3}^e \end{bmatrix}.$$

Then the local matrices are assembled in order to form the global matrices.

$$\sum_{i=1}^n [K_{ij}^e] [a_{ij}^e] = [f_i^e],$$

where n is the number of elements in the domain.

To solve the sets of the global nonlinear algebraic equations in the form of matrix, the Newton-Raphson iteration technique has been adapted through PDE solver with MATLAB interface. The convergence criterion has been set to $|\Psi^{m+1} - \Psi^m| \leq 10^{-4}$, where m is number of iteration.

4.4 Grid independency test

Preliminary results are obtained to inspect the field variables grid independency solutions. Test for the accuracy of grid fineness has been carried out to find out the optimum grid number. It is found in Fig. 2 that 41499 non-regular nodes are sufficient to provide accurate results.

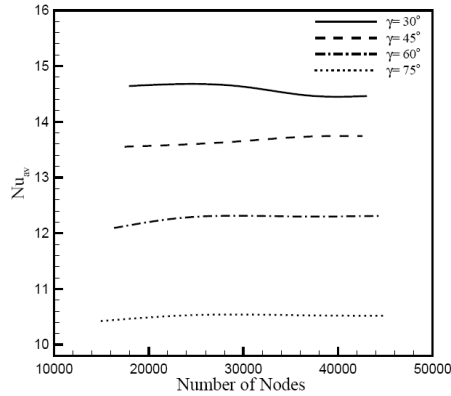


Fig. 2. Grid sensitivity test at $Ra_m = 1000$, $Da = 10^{-6}$ and $\Phi = 0^\circ$.

4.5 Code validation

For the validation of the code, a square porous cavity with differential isothermal vertical walls and adiabatic horizontal walls in the absence of the applied magnetic force is considered. Average Nusselt number is calculated for three different Rayleigh numbers ($Ra_m = 10, 100$ and 1000) while the Darcy number is fixed at 10^{-6} and compared with the available published works by Baytas and Pop [20], Gross et al. [21], Manole and Lage [22], Moya et al. [23] and Mahmud and Fraser [16]. This comparison is shown in Table 1.

Table 1. Comparison of the presented prediction with the existing one.

	Nu_{av}		
	$Ra_m = 10$	$Ra_m = 100$	$Ra_m = 1000$
Baytas and Pop [16]	1.079	3.16	14.06
Gross et al. [17]	–	3.14	13.45
Manole and Lage [18]	–	3.12	13.64
Moya et al. [19]	1.065	2.80	–
Mahmud and Fraser [12]	1.079	3.14	13.82
Present work	1.079	3.115	13.924

Again another comparison between the present prediction and Mahmud and Fraser [16] is carried out at $Ra_m = 1000$ and $Ha = 5$. The streamlines and isotherms, depicted in Fig. 3, are similar and the average Nusselt number obtained by present work is 3.323 which is very close to that ($Nu_{av} = 3.3$) presented by Mahmud and Fraser. It is seen from Table 1 and Fig. 3 that the agreement between the present and previous results is very good. Therefore, the numerical results presented in this paper are very accurate.

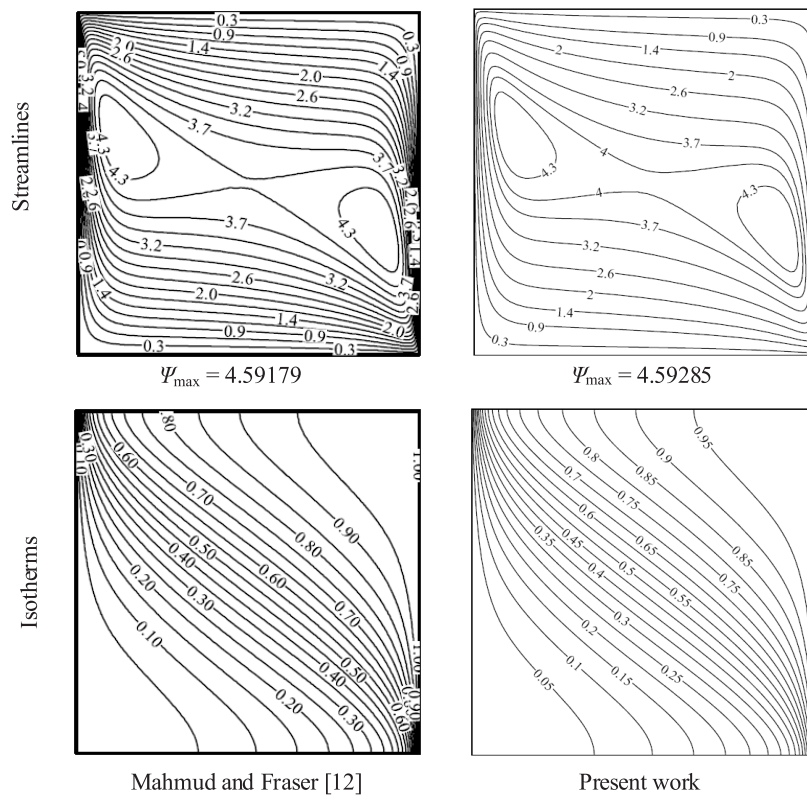


Fig. 3. Code validation at $Ra_m = 1000$, $Ra_f = 10^9$ and $Ha = 5$.

5 Results and discussion

Numerical results are presented in order to determine the effects of the presence of a magnetic field, the modified Rayleigh number, the inclination angles of the sidewalls and the rotational angles of the cavity on natural convection flow of an electrically conducting fluid in a trapezoidal enclosure. The values of the magnetic field parameter Ha range between 0 to 100 and the modified Rayleigh number Ra_m varies from 1 to 1000. The inclination angles of the sidewalls γ , are ranged from 30° to 90° while the rotational angles of the cavity Φ are from 0° to 90° .

5.1 Effect of inclination angles

Fig. 4 reveals the impact of varying inclination angles of the sidewalls of the trapezoidal cavity on buoyancy driven convection for a representative case of $Ra_m = 1000$, $Ra_f = 10^9$ and $\Phi = 0^\circ$. For $\gamma = 30^\circ$, the top cold surface comes closer to the hot wall which squeezes the two counter rotating vortices formed within the cavity. Thereby the core of the circulating cells moves downwards ensuing the development of hydraulic boundary layer on the warm surface. This well-established hydraulic boundary layer ensures the rapid generation of the convective currents. The dense bunch of the isotherms adjacent to the heated wall produces thermal boundary layer, which certainly steps up the convection heat transfer. With increasing the inclination angle of the sidewalls, the core of the circulating rolls moves upward due to the enlargement of the circulation zones, which flattens the hydraulic boundary layer as well as the thermal boundary layer adjoining the

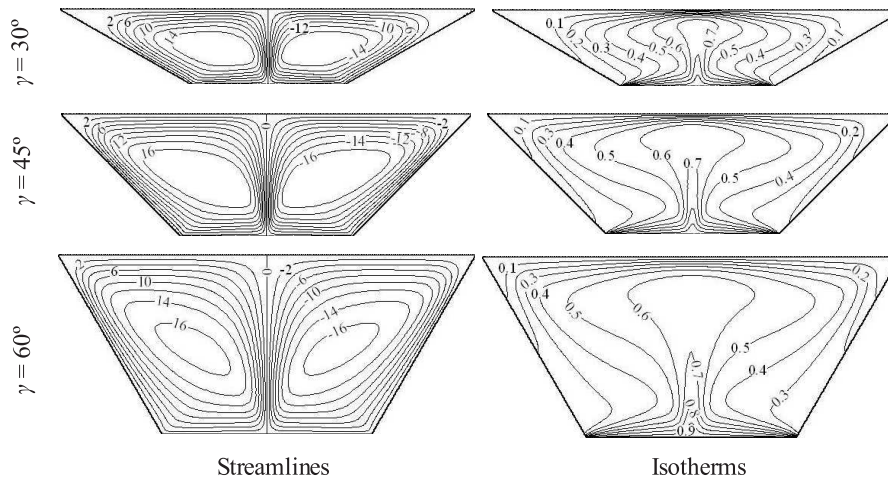


Fig. 4. Streamlines and isotherms at different inclination angles of the sidewalls of the cavity ($Ra_m = 1000$, $Ra_f = 10^9$ and $\Phi = 0^\circ$).

heated bottom wall. Consequently the diffusive flow governs the fluid flow and the heat transportation.

Under the above context, it can be mentioned that amply increase in the convective heat transfer occurs when the inclination angle of the sidewalls of the trapezoidal enclosure γ , is set low.

5.1.1 Optimization test

A theoretical concept can be built for finding out the optimum inclination angle. When two surfaces subjected to differential temperatures are brought closer to each other, the heat transfer rate increases. Under this circumstance if the cold surface extends while it is come closer to the heated surface, the heat transfer rate increases drastically. In case of the heat removal from the nuclear container, the porous saturated trapezoidal enclosure surrounds the container. Thereby the trapezoidal cavity enclosed the container from the top and side should be optimized in context of their inclination angle. It is clear that as the inclination angle of the sidewalls of the trapezoidal enclosure becomes down-sloped, the top surface extends and comes closer to the bottom surface. Thereby the trapezoidal cavities enclosed the container from the top and the sides should be of equal distance between the top and the bottom surfaces of the cavity packed with porous media. Hence the optimum heat transfer performance will be obtained.

Based on this hypothesis, numerical computations have been performed to find out the optimum inclination angle of the sidewalls of the trapezoidal enclosure. The optimization of γ requires to analyze fluid flow and heat transfer characteristics in the cavity at $\Phi = 90^\circ$ as shown in Fig. 5.

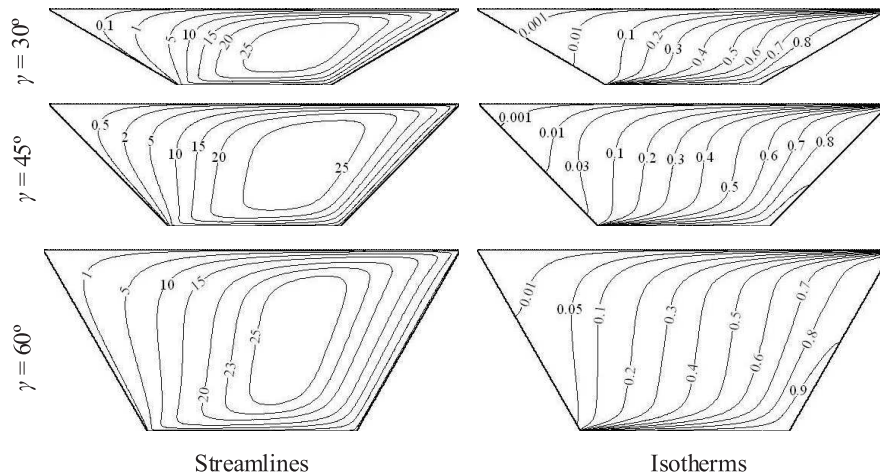


Fig. 5. Streamlines and isotherms at different inclination angle of the sidewalls of the cavity ($Ra_m = 1000$, $Ra_f = 10^9$ and $\Phi = 90^\circ$).

At lower value of γ , a single vortex is formed inside the cavity. The lateral deformation of the circulating cell leads to the growth of the hydraulic boundary layer along the hot surface. The isotherms are also adjusted according to the changes in the flow field and pushed towards the lower part of the right sidewall indicating the presence of a large temperature gradient there. As the inclination angle of the sidewalls increases, the core of the vortex switches towards the left. As a result, the hydraulic boundary layer disappears. Also the vertical stratification of the isotherms at the mid position of the cavity implies that the diffusion is the dominating heat transfer mechanism in the cavity.

Fig. 6 shows the comparison of the average Nusselt numbers obtained from the different combinations of the inclination angles of the sidewalls, γ^t and γ^s mounted on the top and the side of the container. It is found that both of the trapezoidal cavities located at the top and the sides of the container give optimum thermal performance at $\gamma = 45^\circ$.

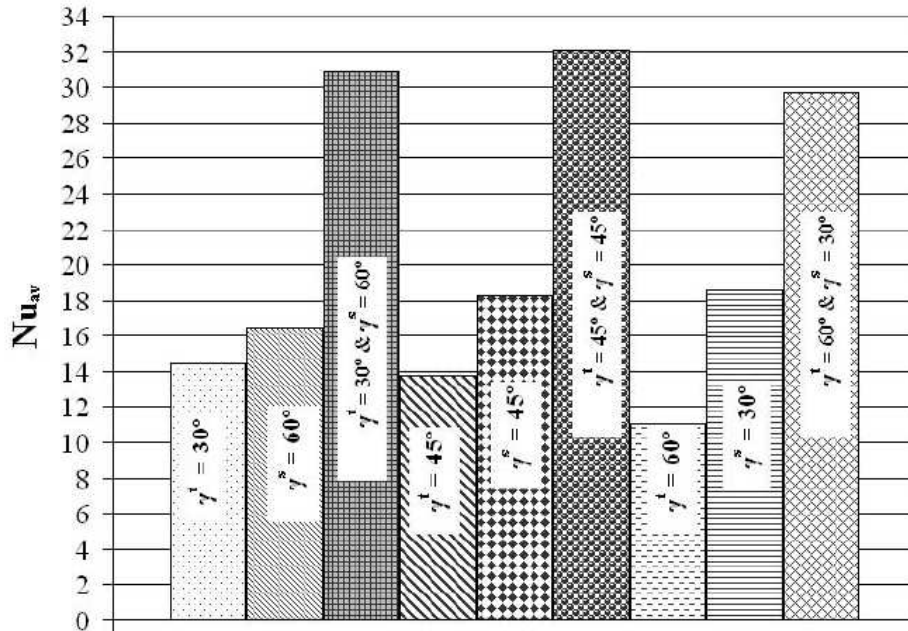


Fig. 6. Selection of optimum inclination angle ($Ra_m = 1000$, $Ra_f = 10^9$, $Ha = 0$ and $\Phi = 0^\circ$).

5.2 Field analysis at optimum inclination angle

5.2.1 Effect of modified Rayleigh number

The evolution of the flow and thermal fields with varying the modified Rayleigh number for different values of Hartmann number and the rotational angle of the trapezoidal cavity is depicted in Figs. 7–18. For the horizontal cavity ($\Phi = 0^\circ$), where the buoyancy force and the applied magnetic force are acting only in the y -direction, the flow domain and

boundary conditions are symmetrical and two counter rotating circulating cells are formed in the cavity. For $Ra_m = 1$ and 100, the flow rises along the vertical symmetry axis and gets blocked at the top isothermal cold wall. Then the flow descends downwards along the inclined adiabatic sidewalls and turns back horizontally to the central region after hitting the bottom wall. The presence of the stagnation point is noticed along the symmetric vertical axis. This type of flow scenario is visualized for the all values of Ha . In the absence of magnetic force, the strength of the recirculating cells is relatively higher. But when the magnetic field is imposed on it, the fluid flow due to buoyancy experiences a retarding force. Therefore the diffusive flow becomes prominent. With an increase in Ra_m up to the moderate value ($Ra_m = 100$), the intensity of the convection increases slightly, the core of the rolls slightly moves towards the symmetric vertical axis. It is noticeable that the strength of the counter clockwise rotating cells is relatively higher than that at low Ra_m . Since the buoyancy forces are more dominant than the viscous forces ensuing due to the magnetic force, the overall convective heat transfer at the moderate Ra_m increases as compared to the low Ra_m . The stratification of the isotherms are found for all values of Ha at $Ra_m = 1-100$, which represents the influence of the viscous diffusion over the convection.

The distinctive hydrodynamic and thermal fields in the cavity at higher Ra_m for different values of Hartmann number are shown in Figs. 15–18. In the absence of any magnetic force ($Ha = 0$), the symmetry may still prevail due to the buoyancy force acting along the direction of the vertical axis. Two circulating cells of higher strength are formed. The isotherms are clustered at the vicinity of the heated wall indicating the existence of thermal boundary layer. At $Ha = 5$, these vortices reduce in strength. As a result, the thermal gradients decrease indicating that the diffusive heat transfer initiates. But multiple primary and secondary vortices rotating in opposite directions to each other are formed within the trapezoidal cavity. The secondary vortices are trapped by the primary circulating cells resulting contraction of the minor cells. The fluid comes from the cold to the hot wall through three channels. Thereby the diffusive currents are still overwhelmed by the convective currents resulting good thermal performance. The isotherms are distorted due to the strong magnetic force. Therefore oscillating thermal boundary layer appears near the heated wall. Higher values of Ha retard the fluid motion which in turns decelerates the convective heat flow and stratify the isotherms which results the reduction in heat transfer rate from the heated surface.

5.2.2 *Effect of rotational angles of the cavity*

For the fair discussion on the variation of the tilted position of the trapezoidal enclosure, a moderate magnetic force ($Ha = 5$) is considered. Figs. 7–18 show the metamorphosis of the thermo-fluid fields under the influence of the rotational angles of the trapezoidal cavity. At lower Ra_m and zero rotational angle, two weaker recirculating cells of opposite directions of motion are developed. The induced buoyancy force is suppressed by the moderate applied magnetic force. As a result, the diffusive heat flow is dominant which reduces the heat transfer performance. Also the stratification of the isotherms reveals the dominance of diffusive heat flux throughout the cavity.

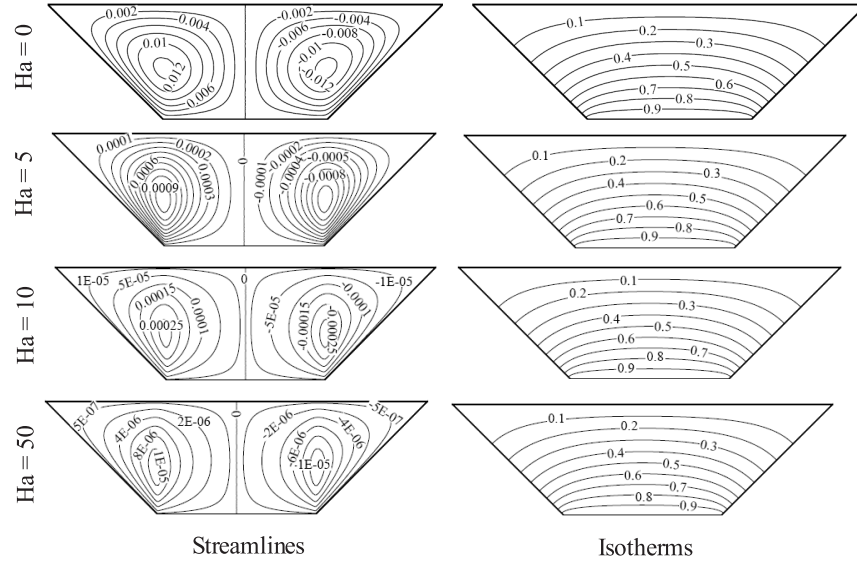


Fig. 7. Streamlines and isotherms for different Hartmann numbers at $\Phi = 0^\circ$, $Ra_f = 10^6$ and $Ra_m = 1$.

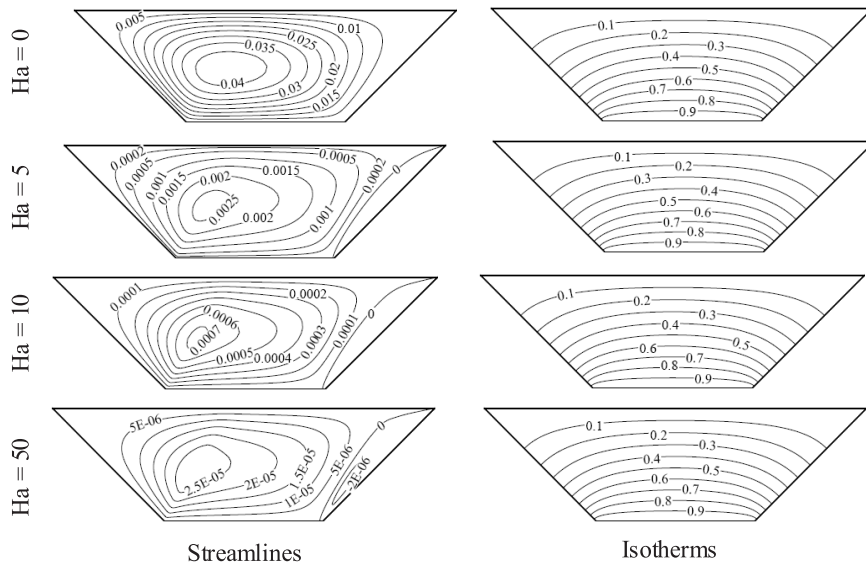


Fig. 8. Streamlines and isotherms for different Hartmann numbers at $\Phi = 30^\circ$, $Ra_f = 10^6$ and $Ra_m = 1$.

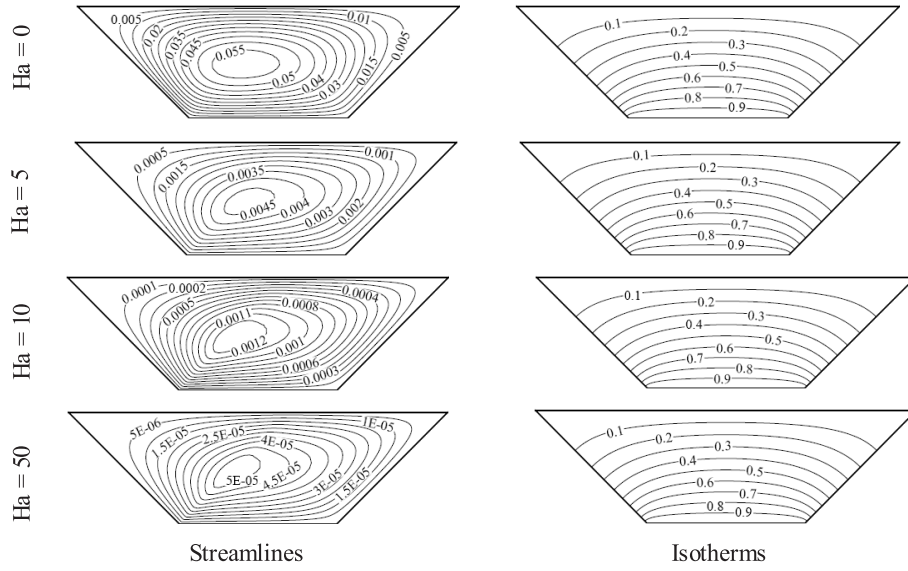


Fig. 9. Streamlines and isotherms for different Hartmann numbers at $\Phi = 45^\circ$, $Ra_f = 10^6$ and $Ra_m = 1$.

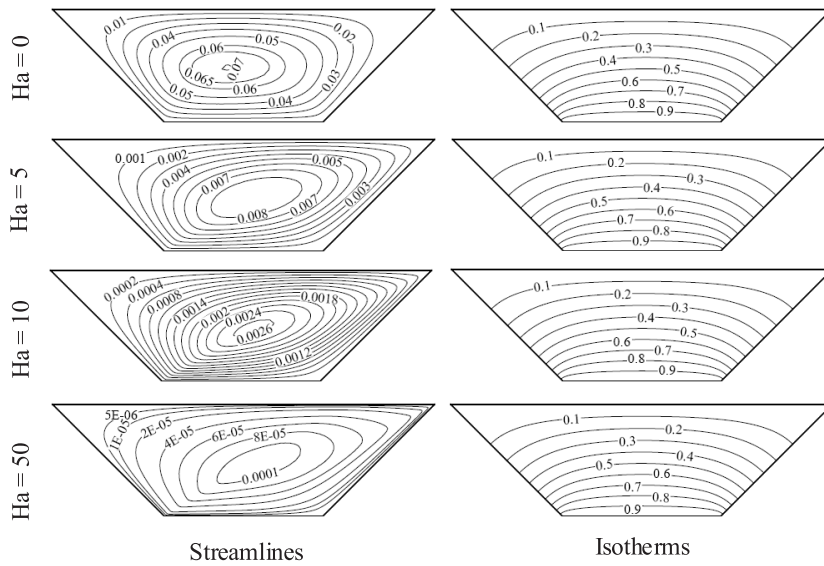


Fig. 10. Streamlines and isotherms for different Hartmann numbers at $\Phi = 60^\circ$, $Ra_f = 10^6$ and $Ra_m = 1$.

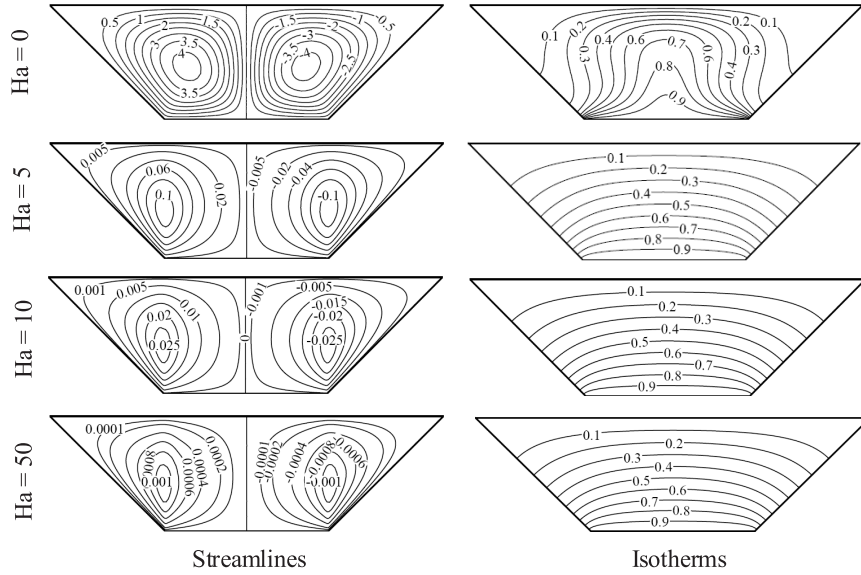


Fig. 11. Streamlines and isotherms for different Hartmann numbers at $\Phi = 0^\circ$, $Ra_f = 10^8$ and $Ra_m = 100$.

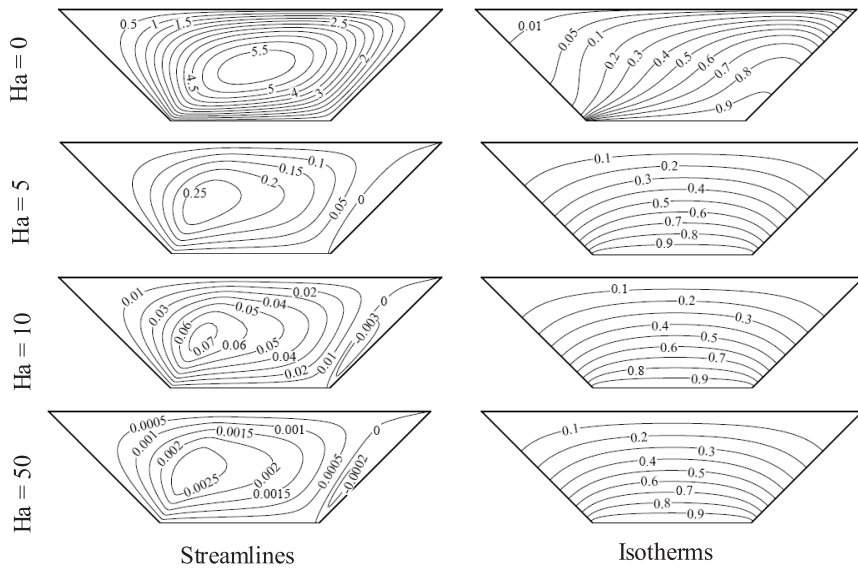


Fig. 12. Streamlines and isotherms for different Hartmann numbers at $\Phi = 30^\circ$, $Ra_f = 10^8$ and $Ra_m = 100$.

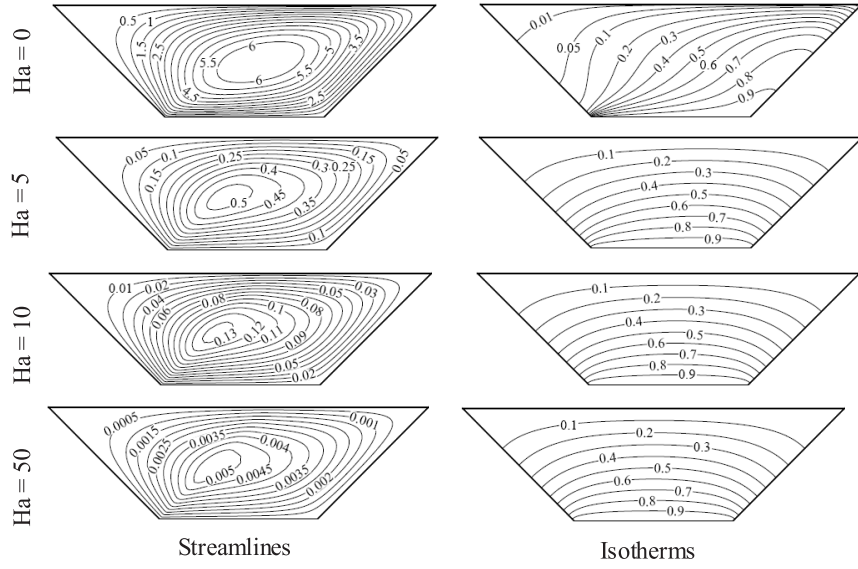


Fig. 13. Streamlines and isotherms for different Hartmann numbers at $\Phi = 45^\circ$, $Ra_f = 10^8$ and $Ra_m = 100$.

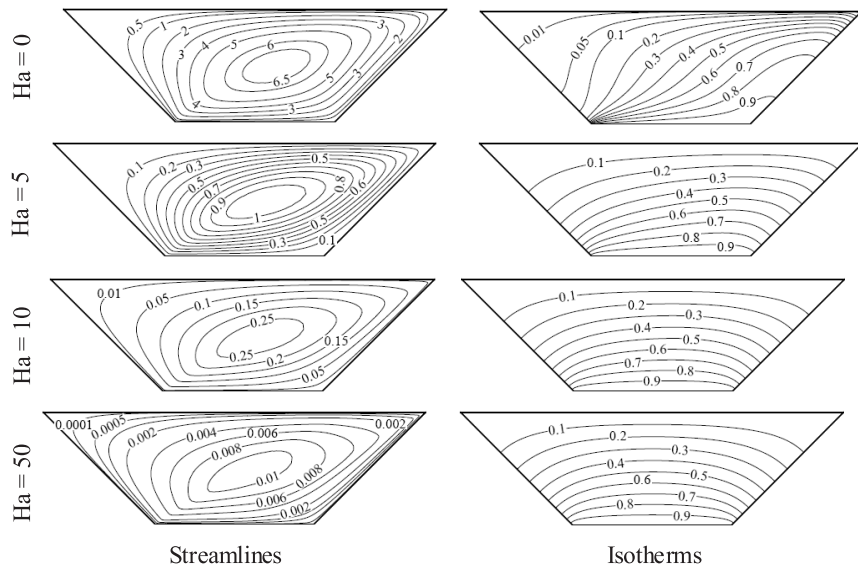


Fig. 14. Streamlines and isotherms for different Hartmann numbers at $\Phi = 60^\circ$, $Ra_f = 10^8$ and $Ra_m = 100$.

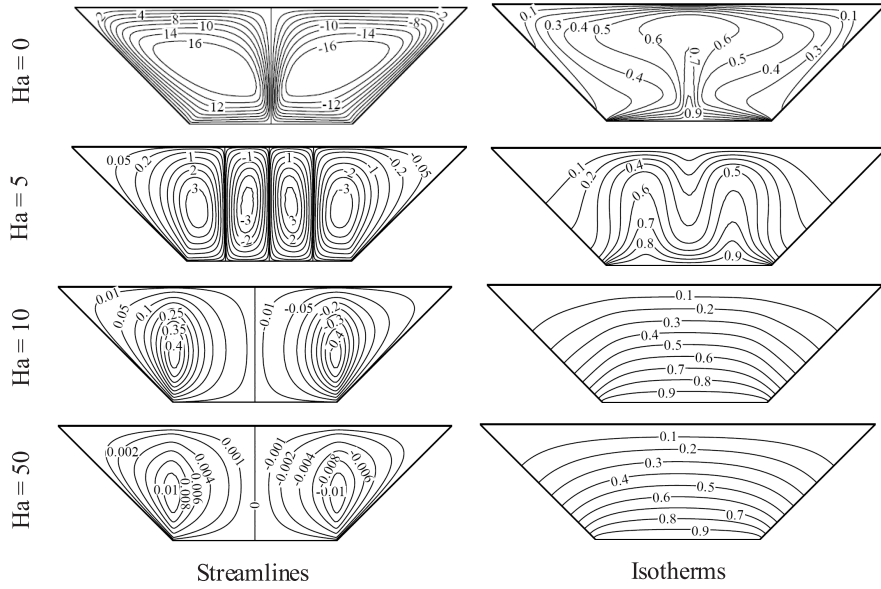


Fig. 15. Streamlines and isotherms for different Hartmann numbers at $\Phi = 0^\circ$, $Ra_f = 10^9$ and $Ra_m = 1000$.

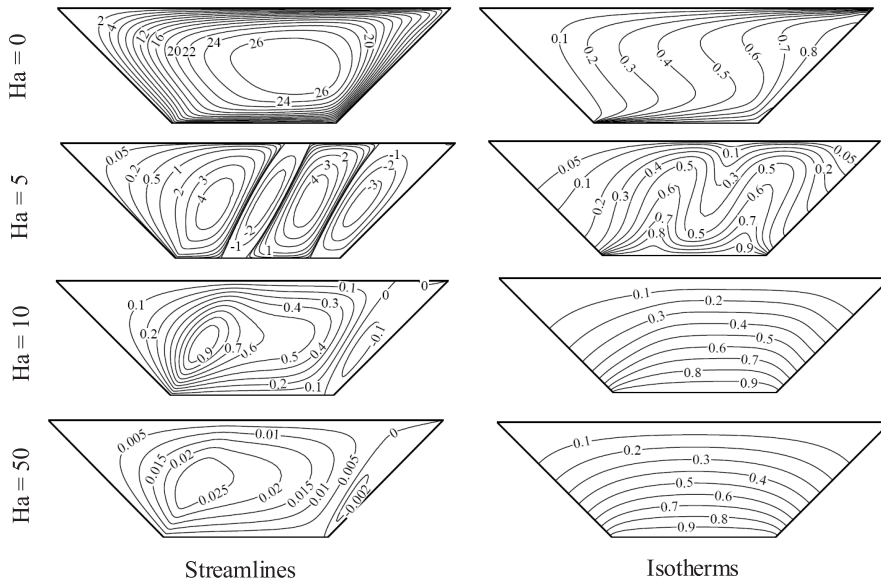


Fig. 16. Streamlines and isotherms for different Hartmann numbers at $\Phi = 30^\circ$, $Ra_f = 10^9$ and $Ra_m = 1000$.

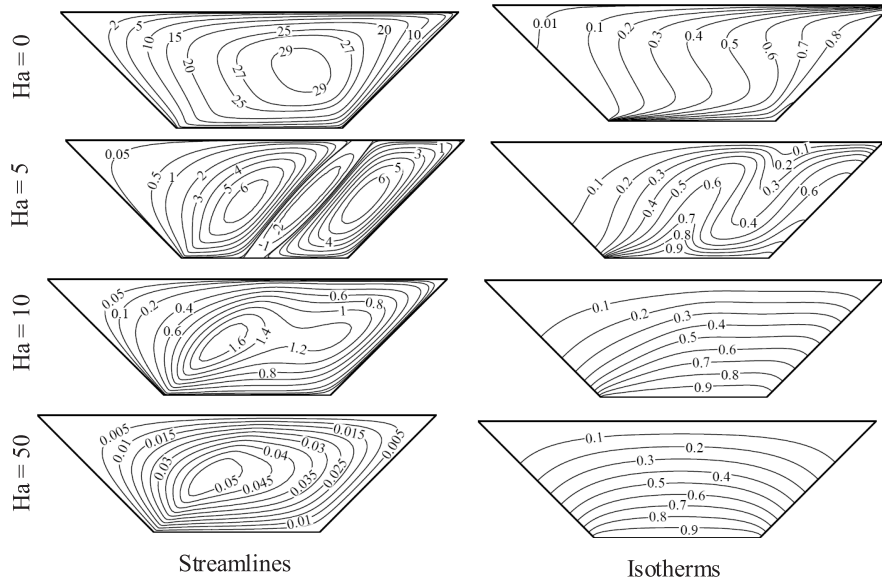


Fig. 17. Streamlines and isotherms for different Hartmann numbers at $\Phi = 45^\circ$, $Ra_f = 10^9$ and $Ra_m = 1000$.

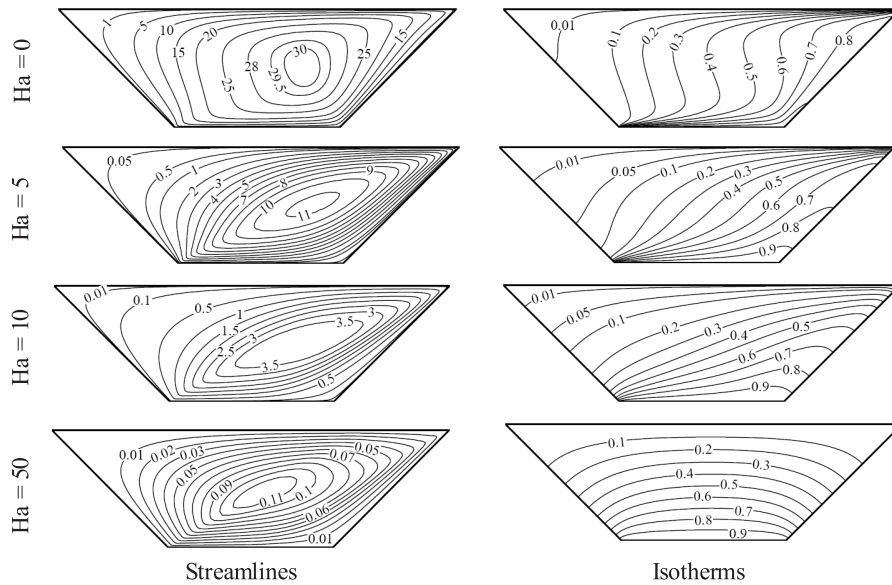


Fig. 18. Streamlines and isotherms for different Hartmann numbers at $\Phi = 60^\circ$, $Ra_f = 10^9$ and $Ra_m = 1000$.

An increase in the rotational angle leads the left circulating cell expands and the right circulating cell squeeze. Here the symmetry is completely destroyed due to the counterbalancing action of the buoyancy force and the imposed magnetic force. The weak magnetic force along the y -direction accelerates the fluid flow even at low Ra_m . Consequently the buoyancy driven convective flow becomes relatively stronger. The isotherms for the lower value of Ra_m still show the thermal stratification. Therefore the convective flow is slightly amplified. For the moderate Ra_m , slight temperature gradients develop when the cavity is tilted at $\Phi = 45^\circ$. After that, as the cavity is tilted at a greater angle, the thermal boundary layer tends to initiate and the flow field tends to stretch diagonally. Thus the convection becomes established. Higher values of Ra_m ($Ra_m = 1000$) give idiosyncratic thermo-fluid attributions. At $\Phi = 0^\circ$, multiple circulating cells are formed and a disturbance is observed in the thermal field. Two maxima and three minima are generated which means that the fluid comes from the cold wall to the hot wall through the minima indicating the supremacy of the convective flow.

Tilting the cavity to an extend yields the left side shipment of the cores of the vortices and the rigorous development of the plumage inside the cavity. As the cavity tilts more, the primary vortex located at the left side grasps the other vortices. Finally a diagonally stretched primary vortex grows within the enclosure, which invokes that the convection is the only means of heat transfer. The isotherms at $\Phi = 45^\circ$ show that the area of the minima increases although its number is decreased. These large temperature gradients establish the oscillating thermal boundary layer at the vicinity of the heated wall. Further increase in Φ concentrates the isotherms towards the hot surface indicating better thermal performance.

5.2.3 Effect of Hartmann number

Figs. 9, 13 and 17 illustrate the changes in the flow and thermal fields due to the variation of the magnetic force for different Ra_m within the cavity while the rotational angle is fixed at 45° . In the absence of magnetic force, a single circulating cell of relatively higher strength and counter clockwise direction of motion is formed at the lower value of Ra_m (Fig. 9). As the intensity of the applied magnetic force increases, the recirculating cell experiences retardation in the motion. The diffusive currents start to dominate the convective currents. When the magnetic force triumphs over the buoyancy force, the core of the vortex shifts the left downward. This stretched vortex cannot flow smooth losing its strength. Viscous diffusion plays an important role there. The isothermal lines are merely symmetrical. The layered isotherms indicate the strong influence of the viscous diffusion.

For the moderate value of Ra_m , when the magnetic force is absent, a strong primary vortex is formed as compared to that at low Ra_m . The intensity of the circulation is due to the influence of buoyancy effect only. The isotherms are clustered near the heated surface-giving rise to a thermal buoyancy layer. Viscous diffusion is outweighed by the convective flow. As the magnetic force is applied sequentially, a large portion of fluid in the mid position of the cavity becomes also motionless. This is supported by the elongated-stagnant core of the vortex with increasing Ha . Also the thermal boundary

layer disappears and the stratification of the isotherms points towards the deceleration of the convective heat flux.

For the higher Ra_m where the buoyancy effects are strong, a comparatively strong vortex of counter clockwise direction is formed in the absence of the magnetic field. The isotherms are extensively nonlinear which indicates the higher temperature gradients. Near the heated wall, the isotherms are bunched to develop thermal boundary layer. This type of thermo-fluid behavior reveals the strong influence of the convective currents. With increasing Ha in a small amount causes the core of the circulation shift right side resulting stagnation point at the left upper corner of the cavity. The isothermal lines also switch towards the right side, decelerating the thermal boundary layer formation. At $Ha = 5$, multicellular formation appears in the cavity. The weaker zone is shifted towards the mid position. This minor vortex is entrapped by the two major vortices. Therefore the diffusive flow becomes prominent. The oscillating thermal boundary layer represents the dominancy of the diffusive heat flux. Over-estimated magnetic force hinders the circulating flow and may cause the mitigation of the convective heat transfer mechanism. The temperature gradients are also straightened which indicates the ostracism of the convective heat flow.

5.3 Heat transfer characteristics

The corresponding effects of the increase of the modified Rayleigh number on the surface heat transfer from the heated surface of the cavity at different values of Hartmann number, Ha , and rotational angle of the cavity, Φ , are presented in Fig. 19. Two distinct zones are identified depending on the value of Ra_m . In the diffusion-dominated zone, the average Nusselt number is invariant of Ra_m and the magnitude of Nu_{av} is equal to 2. In the convection-dominated zone, Nu_{av} increases almost linearly in logarithmic plot with increasing Ra_m . The diffusion-dominated zone is extended with increasing Ha as well as decreasing Φ . In the convection-dominated zone, lower value of Ha and higher value of Φ show a higher value of Nu_{av} .

Variation of the average Nusselt number with Hartmann number at $\Phi = 0^\circ$ and $\gamma = 45^\circ$ as shown in Fig. 20 indicates that the higher convective heat transfer is obtained in the absence of magnetic force. Once the magnetic force is established, the Nu_{av} decreases rapidly and approaches its asymptotic value ($= 2$). For smaller Ra_m , the average Nusselt number approaches the asymptotic value even for the lower values of Hartmann number.

Fig. 21 shows an analogous heat transfer behavior with increasing Hartmann number at $\Phi = 30^\circ$. A slight increase in Nu_{av} with Ha can be found. In Fig. 22, the convection-dominated zone is extended with increase in Ha . The bifurcation point along the asymptotic line switches towards the right with decreasing Ha , indicating that the lower values of Ha extends the diffusion prominent zone. An identical $Nu_{av}-Ha$ profiles are obtained for $\Phi = 90^\circ$ as shown in Fig. 23. The only exception is that the convection is overwhelmed by the diffusion as the applied magnetic force reduces to zero.

Fig. 24 shows the influence of the tilted position of the cavity on the convective heat transfer attributes for different values of Ra_m and Ha . In general, Nu_{av} remains unchanged up to $\Phi = 15^\circ$ indicating that the diffusion is the only principal mode of heat

transfer. Further increase in Φ yields that the buoyancy dominated heat transfer initiates and becomes profound up to $\Phi = 60^\circ$. After that, the convective heat transfer decelerates along with Φ . The optimum convective flux is established at $\Phi = 60^\circ$ and higher values of Ra_m over a wide range of Ha .

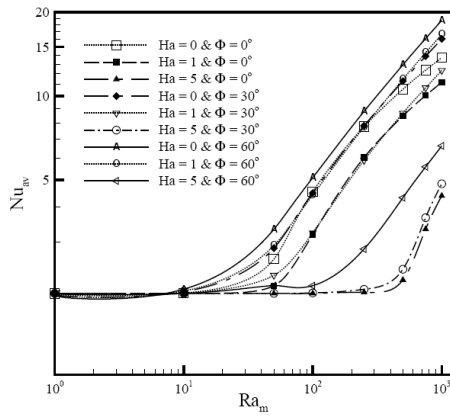


Fig. 19. Variation of average Nusselt number at the heated wall with modified Rayleigh number for $\Phi = 0^\circ, \gamma = 45^\circ$.

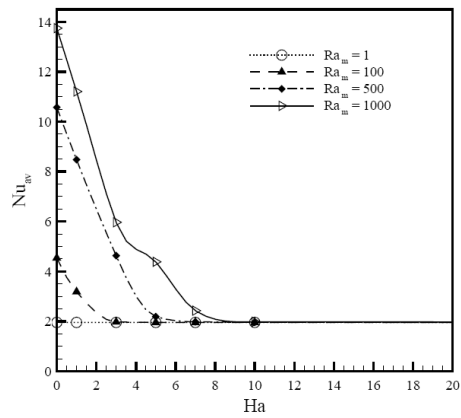


Fig. 20. Variation of average Nusselt number at the heated wall with Hartmann number for $\Phi = 0^\circ, \gamma = 45^\circ$.

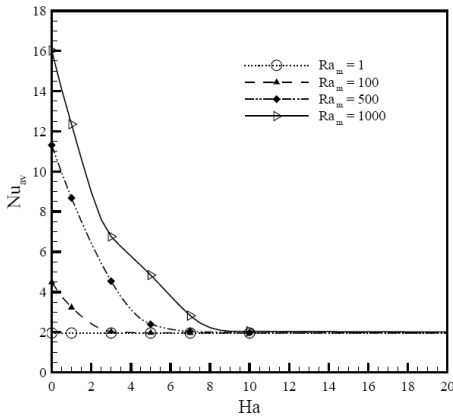


Fig. 21. Variation of average Nusselt number at the heated wall with Hartmann number for $\Phi = 30^\circ, \gamma = 45^\circ$.

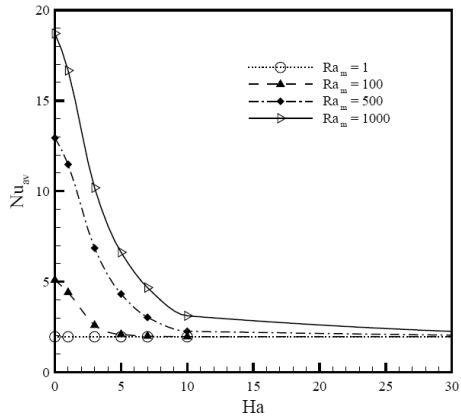


Fig. 22. Variation of average Nusselt number at the heated wall with Hartmann number for $\Phi = 60^\circ, \gamma = 45^\circ$.

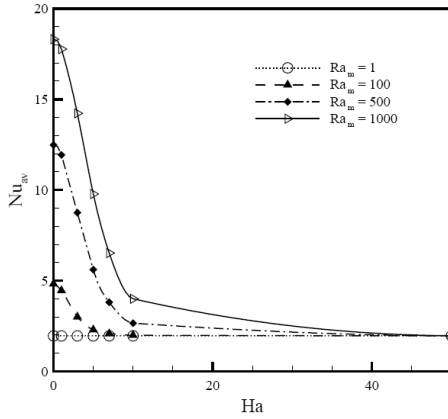


Fig. 23. Variation of average Nusselt number at the heated wall with Hartmann number for $\Phi = 90^\circ, \gamma = 45^\circ$.

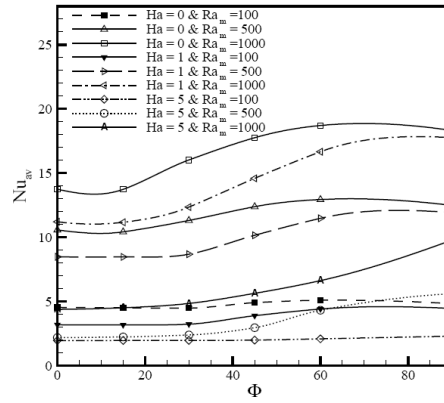


Fig. 24. Variation of average Nusselt number at the heated wall with rotation angle of the cavity.

6 Conclusion

Two dimensional, steady natural convection flow in a trapezoidal cavity, packed with porous medium and subjected to isothermal boundary conditions at the horizontal walls and adiabatic conditions at the inclined sidewalls, has been studied numerically for a wide range of the modified Rayleigh number, the inclination angles of the sidewalls of the cavity, the rotational angles of the cavity and the Hartmann numbers. A numbers of conclusions can be drawn from the investigation:

At moderate value of Ra_m , when the inclination angles of the sidewalls of the enclosure are small, a well-established thermal boundary layer is found near the heated wall which indicates that the convective flow is profound there. With increasing γ , the thermal boundary layer is broken and finally it disappears causing strong diffusive currents. An optimization test has been performed by considering a physical problem of the nuclear waste removal. It is notice worthy that the optimum thermal performance is achieved at $\gamma = 45^\circ$.

At lower value of Ra_m , the thermal stratification inside the cavity indicates that the convection is overwhelmed by the conduction mechanism whereas the convection-dominated zone is established at higher values of Ra_m .

In the absence of the magnetic force, the convection-dominated zone is extended resulting better convective heat transfer performance. Increasing Hartmann number retards the fluid circulation causing the lower temperature gradients throughout the cavity. Therefore, major portion of the heat is transferred mainly by conduction.

With an increase in the tilted position of the cavity up to 60° , the average Nusselt number increases pointing towards the supremacy of the convective currents over the diffusive flows. Further increase in the rotational angle of cavity causes slight decrease in average Nusselt number.

References

1. J. Bear, *Dynamics of Fluids in Porous Media*, American Elsevier publishing company, Inc., New York, 1972.
2. D.A. Nield, A. Bejan, *Convection in Porous Media*, 3rd ed., Springer, New York, 2006.
3. *Transport Phenomena in Porous Media*, D.B. Ingham, I. Pop (Eds.), Elsevier, Oxford, 2005.
4. *Hanbook of Porous Media*, K. Vafai (Ed.), 2nd ed., Taylor & Francis, Boca Raton, 2005.
5. *Emerging Topics in Heat and Mass Transfer in Porous Media*, P. Vadasz (Ed.), Springer, New York, 2008.
6. I. Pop, D.B. Ingham, *Convective Heat Transfer: Mathematical and Computational Modeling of Viscous Fluids and Porous Media*, Pergamon, Oxford, 2001.
7. H. Bénard, Formation périodique de centres de giration à l'arrière d'un obstacle en mouvement, *C. R. Acad. Sci.*, **147**, pp. 839–842, 1908.
8. L. Rayleigh, On convection currents in a horizontal layer of fluid when the higher temperature is on the underside, *Philos. Mag.*, **6**(32), pp. 529–546, 1946.
9. H. Jeffreys, Some cases of instabilities in fluid motion, *P. Roy. Soc. Lond. A Mat.*, **118**, pp. 195–208, 1928.
10. N.H. Saied, I. Pop, Non-Darcy natural convection in a square cavity filled with a porous media, *Fluid Dyn. Res.*, **36**, pp. 35–43, 2005.
11. F. Marcondes, J.M. Medeiros, J.M. Gurgel, Numerical analysis of natural convection in cavities with variable porosity, *Numer. Heat Tr: A-Appl.*, **40**, pp. 403–420, 2001.
12. P. Nithiarasu, K.N. Seetharamu, T. Sundararajan, Numerical investigation of buoyancy driven flow in a fluid saturated non-Darcian porous medium, *Int. J. Heat Mass Tran.*, **42**, pp. 1205–1215, 1999.
13. E. Baez, A. Nicolas, 2D natural convection flows in tilted cavities: Porous media and homogeneous fluids, *Int. J. Heat Mass Tran.*, **49**, pp. 4773–4785, 2006.
14. A.C. Baytas, I. Pop, Natural convection in a trapezoidal enclosure filled with a porous medium, *Int. J. Eng. Sci.*, **39**, pp. 125–134, 2001.
15. F.C. Lai, I. Pop, Natural Convection in a Truncated Circular Sector of Porous Medium, *Int. Commun. Heat Mass*, **17**, pp. 801–811, 1990.
16. S. Mahmud, R.A. Fraser, Magneto-hydrodynamic free convection and entropy generation in a square porous cavity, *Int. J. Heat Mass Tran.*, **47**, pp. 3245–3256, 2004.
17. T.S. Lundgren, Slow flow through stationary random beds and suspensions of spheres, *J. Fluid Mech.*, **51**, pp. 273–299, 1972.
18. T. Levy, Loi de Darcy ou loi de Brinkman?, *C. R. Acad. Sci. II*, **292**, pp. 872–874, 1981.
19. J.N. Reddy, D.K. Gartling, *The Finite Element Method in Heat Transfer and Fluid Dynamics*, CRC Press, Inc., Boca Raton, Florida, 1994.

20. A.C. Baytas, I. Pop, Free convection in oblique enclosures filled with a porous medium, *Int. J. Heat Mass Tran.*, **42**, pp. 1047–1057, 1999.
21. R.J. Gross, M.R. Bear, C.E. Hickbox, The application of flux-corrected transport (FCT) to high Rayleigh number natural convection in porous media, in: *Proc. 8th Int. Heat Transfer Conference, San Francisco, CA, 1986*.
22. D.M. Manole, J.L. Lage, Numerical benchmark results for natural convection in a porous medium cavity, in: *Heat and Mass Transfer in Porous Media, ASME Conference, HTD-216*, pp. 50–60, 1992.
23. S. Moya, E. Ramos, M. Sen, Numerical study of natural convection in a tilted rectangular porous material, *Int. J. Heat Mass Tran.*, **30**(4), pp. 741–756, 1987.